Additive Manufacturing Frontiers 4 (2025) 200236

Contents lists available at ScienceDirect

Additive Manufacturing Frontiers

journal homepage: www.elsevier.com/locate/amf

Thermal variables evolution inside melt pool during LPBF of 316L stainless steel: A numerical approach

Saad Waqar[a,*], Hamaid M. Khan[b], Aamer Nazir[c], Changyong Chen[d,*], Usama Waleed Qazi[e], Hassan Ejaz[f]

[a] Department of Mechanical Engineering, Politecnico di Milano, Milan, Italy
[b] Aluminum Test Training and Research Center (ALUTEAM), Fatih Sultan Mehmet Vakif University, Istanbul, Turkey
[c] Department of Mechanical Engineering, King Fahd University of Petroleum & Minerals, Dhahran, Saudi Arabia
[d] Department of Industrial and Systems Engineering, Hong Kong Polytechnic University, Hong Kong, China
[e] Air University School of Management, Air University, Islamabad, Pakistan
[f] Mechanics of Composites for Energy and Mobility Lab, King Abdullah University of Science and Technology, Thuwal, Saudi Arabia

ARTICLE INFO

Keywords:
Laser powder bed fusion
Finite element method
Melt pool
Microstructure
Thermal profile

ABSTRACT

The anisotropy of LPBF fabricated components is a serious concern and often increases the overall production cost by creating the necessity for secondary thermal homogenization processes. The microstructural features are the main driving force behind these anisotropic behaviors. Whereas the unique and distinctive thermal history inside a melt pool and its transient transformation is the reason for the characteristic microstructural features of LPBF fabricated components. Therefore, this paper investigates the prominent thermal variables such as heating rate, cooling rate, solidification rate etc., and their evolution inside the melt pool of 316 L stainless steel during LPBF process to provide a reference for further exploring the generation of various microstructural features. A numerical model for macroscale investigation of thermal behavior inside melt pool was established. A 3D Gaussian heat source model coupled with temperature and density dependent properties of powder and solid phase 316 L stainless steel was used. The variation and evolution of significant thermal variables inside the melt pool were then investigated with the established numerical model. The study found that the Gaussian profile of a laser beam influences the thermal variables inside a melt-pool, including cooling rates, solidification rates, and thermal gradients. The nodes lying under the laser edge receive less heat, resulting in higher cooling effects, which shapes the grain morphology. Finer grains can be formed near the bottom melt front as well as at the center of the melt-pool surface. However, reheating adjacent tracks can result in grain coarsening. Since the generation of microstructural features is dominantly dependent on the thermal behavior inside the melt pool, an assessment of these variables is important and provides basics for the understating of different features generated in the LPBF processed components.

1. Introduction

Laser powder bed fusion (LPBF) is a state of the art additive manufacturing (AM) technique that has the potential to fabricate intricate geometrical components in a layer by layer fashion [1,2]. The LPBF process involves melting of micro-scale partials of metallic materials or their alloys under the influence of high power laser beams acting as heat source [3]. Since most of metallic materials and their alloys have high melting points i.e., in the range of 1200 °C to 1800 °C, the temperature requirements for complete and homogeneous melting are even beyond this range [4,5]. The transition of powder particles from room temperature to such a high temperature in a short span of time followed by the subsequent cooling back to ambient temperature is a complicated phenomenon that has the tendency to alter the behavior of fabricated components [6,7]. Given the layer-by-layer manufacturing nature, anisotropy is one of the main concerns in LPBF process as the behavior and properties of fabricated components vary along different axis [8,9]. A thorough understanding of such anisotropy is of paramount importance so that it can be catered for during the fabrication and design phase for LPBF fabricated components. Since the anisotropy of LPBF fabricated components is either directly (microstructure, defects, residual stresses) [9,10] or indirectly (hardness, strength, distortion) [11–13] associated with the thermal gradient and thermal variables especially inside the melted region at a given instance, the correlations between variables and thermal gradients along different axis should be investigated in detail.

* Corresponding authors.
E-mail addresses: saad.waqar@polimi.it (S. Waqar), cychenhk1@gmail.com (C. Chen).

https://doi.org/10.1016/j.amf.2025.200236
Received 27 November 2024; Received in revised form 16 June 2025; Accepted 23 June 2025
Available online 26 July 2025

Since the observation of evolution of thermal behaviors during LPBF process is complex and often impossible with existing experimental facilities, numerical modeling approaches are a cost-effective alternative. Several studies have been reported in the existing literature regarding the numerical investigations of thermal behaviors governing the LPBF process. Li et al. [14] numerically investigated the thermal distribution, powder to liquid and solid phase transitions. The attained results showed good correlations between experimental and numerical outcomes and hence endorse the selection of numerical approach for predicting thermal behaviors. Gusarov et al. [15] applied a 3D volumetric heat source to simulate the LPBF process of 316L stainless steel and observed the melt pool morphology and thermal gradient under different processing parameters. Mishra et al. [16] studied the melt pool morphology and distribution for LPBF of Ti6Al4V. They used 2D gaussian heat source, Gaussian exponential volumetric heat source and egg shape volumetric heat source. Patil et al. [17] developed a thermal model to predict the thermal distribution during the laser sintering of a powder uni-layer. Matsumoto et al. [18] proposed a combined model to predict thermal and stress profile that considers the elastic deformations occurring during the process as well. Loh et al. [19] investigated the evolution of melt pool geometry as well as the thermal profile change for aluminum alloy 6061. The influence of various processing parameters were also investigated. Heeling et al. [20] adopted numerical modeling to evaluate the LPBF process for a uni-layer and uni-track model. The established numerical model also considered the influences of evaporation as well as powder layer absorptivity. Liu et al. [21] used a single-track multi-layer simulation to investigate the subsequent thermal cycling phenomenon existing during SLM process. Zhang et al. [22] developed a single-layer multi-track model by considering both the thermal heat transfer and fluid flow models for an estimation of thermal behavior inside the melt pool. Li et al. [23] proposed a uni-layered FEM model to investigate thermal and stress fields in SLM-fabricated thin-walled components.

Based on the literature review it was observed that although several investigations have been carried out to observe the thermal behavior during LPBF process and to establish correlations between process variables and thermal phenomena, however a large proportion of these investigations only worked on macro level behaviors, i.e., a unified value for a specific instance. These results are good in predicting and estimation of part scale behaviors like residual stresses, distortions, and deformations [24–26]. However, there are several other parameters that cannot be directly associated with macro level thermal behaviors. For instance, microstructure features and grain morphology depend highly on the thermal profile inside melt pool [27,28]. The thermal distribution and thermal variables inside a melt pool are not well-researched despite their evident importance in predicting the micro level features of fabricated components.

Therefore, in the present work an attempt has been made to analyze the thermal distribution inside the melt pool i.e., the change in thermal profile inside a melt pool during LPBF process. Numerical modeling approach through finite element method (FEM) was adopted for the aforementioned investigation. The melt pool thermal distribution along different axis, cooling rate, and solidification rate are the prominent variables that were investigated. The results obtained from the present investigation can form the basis for the generation of various grains and microstructural features in LPBF fabricated components.

2. Numerical Modeling Methodology

2.1. Heat transfer, thermal and material governing equations

The classical heat transfer equation with Fourier series can be stated as Ref. [6].

$$\frac{\partial}{\partial x}\left(k_x(T)\frac{\partial T}{\partial x}\right)+\frac{\partial}{\partial y}\left(k_y(T)\frac{\partial T}{\partial y}\right)+\frac{\partial}{\partial z}\left(k_z(T)\frac{\partial T}{\partial z}\right)+Q=\rho(T)C(T)\frac{\partial T}{\partial t}\ . \tag{1}$$

By considering a continuum approach and uniform anisotropy along different axis, Eq. (1) can be simplified as:

$$k(T)\frac{\partial^2 T}{\partial x^2}+k(T)\frac{\partial^2 T}{\partial y^2}+k(T)\frac{\partial^2 T}{\partial z^2}+Q=\ \rho(T)C(T)\frac{\partial T}{\partial t}. \tag{2}$$

The initial temperature of model was assumed equivalent to ambient temperature T_0 (i.e., 25 °C).

$$T(x,y,z,t)|_{t=0}=T_0(x,y,z). \tag{3}$$

Considering all three heat transfer modes i.e., radiation, conduction and convection, thermal equilibrium can be achieved as stated by Eq. (4)

$$k\left(\frac{\partial T}{\partial n}\right)+h\left(T-T_0\right)+\varepsilon\sigma\left(T^4-T_0^4\right)-q=0. \tag{4}$$

In order to accurately model the laser material interaction a modified 3D heat source model with Gaussian distribution was used, which can be stated by Eq. (5).

$$Q=\frac{2\eta P}{\pi R^2 S}\exp\left(-\frac{2\left((x-vt)^2+y^2\right)}{R^2}\right)\exp\left(\frac{-|z|}{S}\right), \tag{5}$$

where η is laser absorptivity of material, P is laser power, S is laser penetration depth in material, and R is the laser beam radius corresponding to the point where laser irradiance diminishes to $1/e^2$. Since in powder phase, the density is not analogous to solid phase and powders are not always closely packed therefore density of the model in powder phase was used as a function of solid phase density, and given by following equation.

$$\rho_p=(1-\varphi)\rho_s, \tag{6}$$

where ρ_p is powder phase density, ρ_s is solid phase density, and φ is the percentage porosity of powder bed. Similarly, conductivity was also adopted to be a function of conductivity given by a relationship as shown in Eq. (7):

$$k_p=(1-\varphi)^4 k_s, \tag{7}$$

where k_p is thermal conductivity of powder phase, k_s is thermal conductivity of solid phase, and φ is the percentage porosity of powder bed. Temperature dependent behavior of 316L stainless steel was also incorporated to the developed model with the help of user defined subroutines. The temperature dependent thermal properties of 316L stainless steel are also given in Fig. 1.

2.2. Model description, meshing sequence and workflow

A complete 3D model i.e., multiple layers and multiple tracks LPBF process-based FEM model was constructed using commercial software package ABAQUS. The dimensions of substrate in FEM model are 1.5 mm × 1.5 mm × 0.5 mm, whereas the dimensions of scanning region are 1 mm × 1 mm × 0.12 mm with 4 powder layers. Thickness of each powder layer is uniformly kept at a value of 30 μm. In order to enhance accuracy and decrease computational cost simultaneously, powder bed region is fine meshed with 25 μm × 25 μm × 15 μm elements. Mesh sizing are also presented in Fig. 2. Whereas, the substrate is fine meshed near to scanning region and relatively coarsely meshed away from scanning region. This meshing strategy has been widely used in various previously published literatures. Heat transfer brick element DC3D8 is used for all the elements in powder bed as well as substrate. Two Fortran based user subroutines namely USDFLD and DFLUX were also used for customized laser and phase control during the LPBF process. USDFLD subroutine was designed to change the phase composition of nodes from powder phase to molten and subsequently solidified, whereas DFLUX is used to cater for predefined heat source distribution as well as laser movement paths. The simulation was performed on uniform processing parameters i.e., scanning speed of 600 mm/s, laser power of 200 W and hatch spacing of 50 μm.

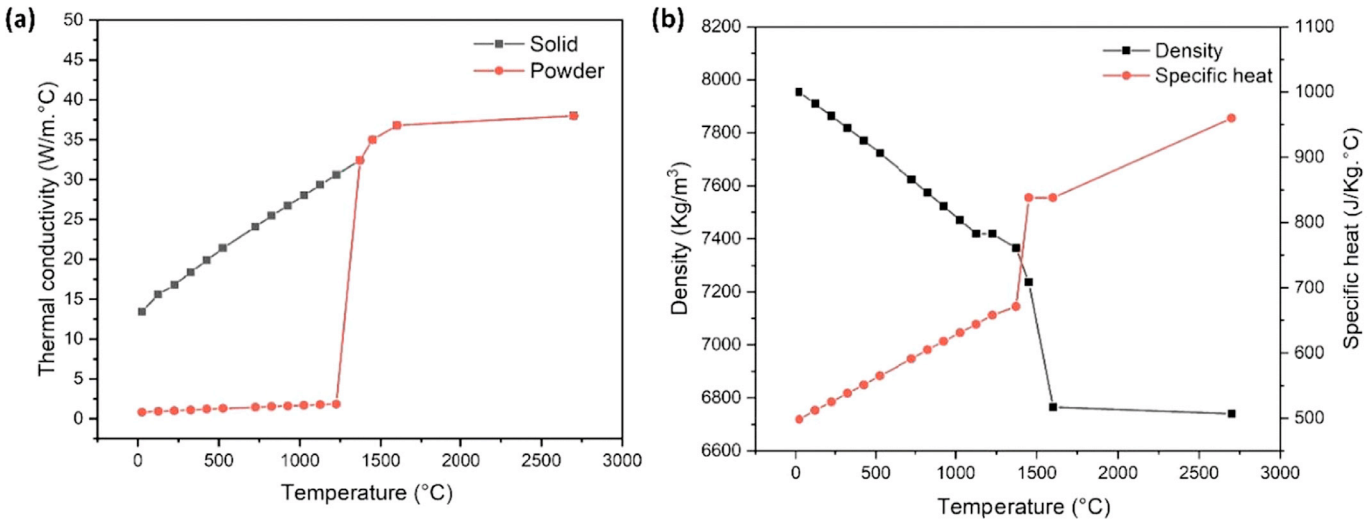

Fig. 1. Temperature-dependent material properties of the 316L stainless steel: (a) Thermal conductivity; (b) Density and specific heat.

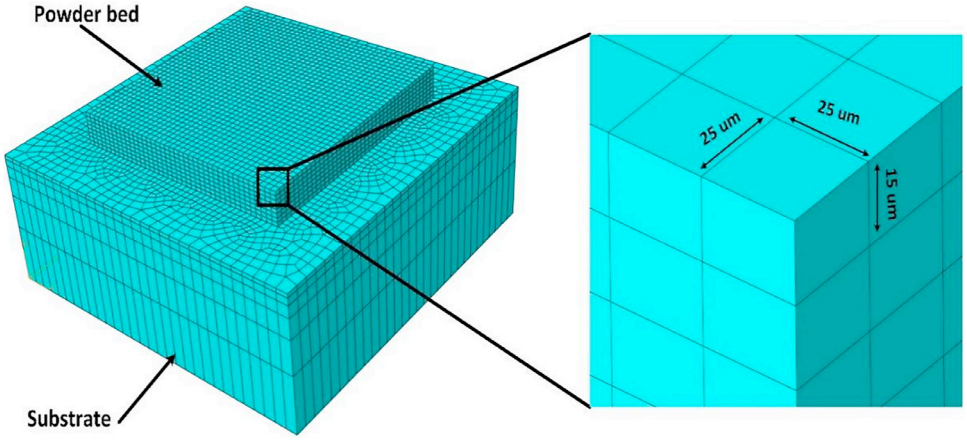

Fig. 2. Numerical model and mesh sizing.

3. Results

3.1. Temperature and cooling rate behavior

The unique manufacturing ways of the LPBF process is a reason for the formation of non-homogenous microstructure in additive components [29]. As the evolution of grains inside a solidifying melt-pool has a strong influence on the final physical, mechanical and electrochemical performance of additively manufactured components, therefore it is academically important to understand and critically analyze the variation of thermal variables inside the melt-pool, such that the process methodology and its influence can be best described. This study intends to discuss the thermal variables evolution, such as nodal temperature, cooling rate, thermal gradient, solidification rate, grain morphology, and size and shape of the melt-pool, as the laser scans the powder bed. This study is a part of our previous work, which focuses on the overall thermal and residual stress behavior of the LPBF process at different laser processing conditions. Overall, 21 tracks and 4 layers were created and simulated to model the actual thermo-mechanical conditions of the LPBF process. The monitored location (i.e., node N-5191) of the present study is on the middle track of the first layer at $X = 0.75$, $Y = 0.75$, $Z = 0.53$ mm, and the processing conditions were kept at 200 W laser, a 600 mm/s scanning speed, 60 μm hatch spacing, and 60 μm laser beam diameter. Since 316L stainless steel has a high melting point of approximately 1380 °C; thus, a high laser power of 200 W is used to generate a complete powder melting within a laser spot to obtain a strong consolidated structure. As shown in Fig. 3(a), the temperature of a node (N-5191) can be seen changing with time, as the laser continue to scan new tracks and layers. The maximum temperature reach for the monitoring node was found at approx. 2661 °C, Fig. 3(b). Overall, the maximum temperature reach of a node was found to reduce with layers but the temperature retention was observed to rise with every layer. This behavior can also be seen in Fig. 3(c), where the surrounding temperature keeps increasing as well as area proportion of that temperature also increases. The rise in temperature retention of a node after each layer can be ascribed to the continuous heat transfer from the layers above and a reduced heat conduction of 316L SS material at lower temperatures. During the scanning of layer 2, the temperature of a node rises again above the melting point. This signifies the node remelting during the LPBF process, which is an ideal case and desirable for good layer to layer consolidation and to achieve a complete melting of powders inside the melt-pool. Moreover, during the scanning of layers 3 and 4, the node temperature approaches 1000 °C, which signifies continuous node reheating throughout the LPBF process. This node reheating can be adequate to nucleate some key intermetallic particles of nano size for high mechanical strength. Reheating is typically influential to homogenize non-equilibrium LPBF microstructure, such as grain refinement and secondary particles formation [30]. However, the limited exposure of few micro-seconds to a high temperature may not be significant to alter the microstructure. On the other hand, the high temperature of a node of about 300 – 500 °C during the

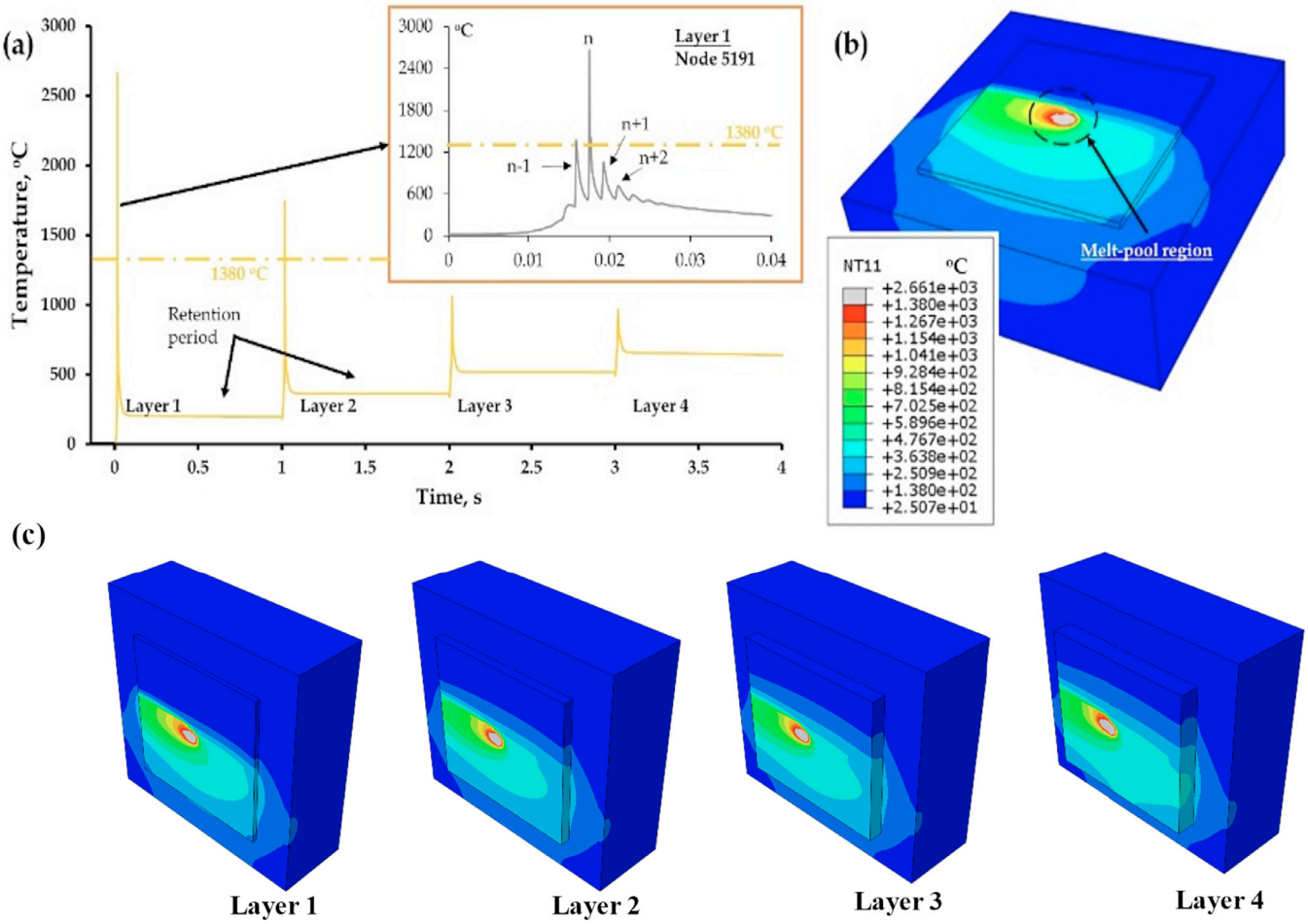

Fig. 3. Time-temperature distribution of a monitored node, N-5191, throughout (a) multiple layers with first layer (inset) and (b) a thermo-mechanical model with a melt-pool, (c) Melt pool model for the subsequent layers.

retention period can be vital to make important changes in the overall mechanical behaviors such as residual stress reduction [31,32]. In the present case of four layers, the retention temperature is observed rising with layers; however, studies have shown that the retention temperature homogenizes when more layers are added [26]. It is because of the continual rise in layer distance from the substrate, such that the temperature dissipation normalizes after the fabrication of some layers.

The inset of Fig. 3(a) shows the instantaneous time-temperature graph of a node during the scanning of layer 1. Here, the peak "n" shows the instantaneous track length, while "n–1" describes the track before and "$n + 1$" denotes the succeeding track, and so on. During the scanning of the previous track, the temperature peak "$n - 1$" of a node can be seen slightly crossing the melting point mark. On the other hand, peaks "$n + 1$", "$n + 2$", and so on can be seen diminishing as the laser scans the succeeding track on the first layer. Multiple temperature peaks of a node signify its continuous re-melting and re-heating throughout the laser scanning process. This behavior can be endorsed by the fact that the thermal conductivity of un melted powder particles is significantly low. Since during the melting of "n" point "$n + 1$" and "$n + 2$" are in powder form and have low thermal conductivity values this results in only a preheating cycle experienced by these points and they do not undergo complete or even partial melting. On the other hand, point "$n - 1$" is in solidified state and also at an elevated temperature which results in high conductivity values and therefore it undergoes complete melting.

Cooling rate is also another important thermal variable that describes the heating and cooling behavior of a node over a time. While Fig. 4(a) shows the cooling rate behavior on multiple layers, Fig. 4(b) describes it on the first layer and near the middle track. The positive values on the Y-axis describe the heating rate and the negative one shows the cooling rate of a node. As noticed, the heating and cooling rates are in the range of $10^6 - 10^7$ °C/s, and this is strongly influenced by the distance between the laser and the node. When new layers are added, the heating and cooling rates of a node continue to drop due to the high heat accumulation, Fig. 3(a). Similarly, during the laser scanning of layer 1 in Fig. 4(b), the heating and cooling rates were highest only when the laser was above the monitoring node, i.e. on track "n". Compared to the peak of "$n + 1$", cooling or heating rate peak "n–1" was higher despite being at the same distance from track "n". It was because the monitoring node (N-5191) was not storing any heat accumulation during the previous track scanning ("n–1"), which was not the case when subsequent tracks, "$n + 1$", "$n + 2$", and so on, were scanned. Fig. 4(c) shows the heating and cooling rate behaviors of a monitoring node at a time when the laser scans it. Compared to the cooling rate, the heating rate was nearly twice it, albeit with a smaller heating window. This shows that the heat addition is rapid that last only for few micro-seconds while the heat dissipation is considerably slow mainly because laser act is external heat source during the heating phase whereas during cooling phase no additional assistance except natural heat transfer phenomena exist. Moreover, the poor heat dissipation through the solidified metal structure and a loosely packed surrounding powder also contributes to the slow cooling rates in comparison with heating rate. In Fig. 4(c), besides the major peaks of heating and cooling rates, some smaller peaks (Pc-1 & Pc-2) associated to a phase change between the solid and liquid phases are also visible. During the instantaneous laser scanning of

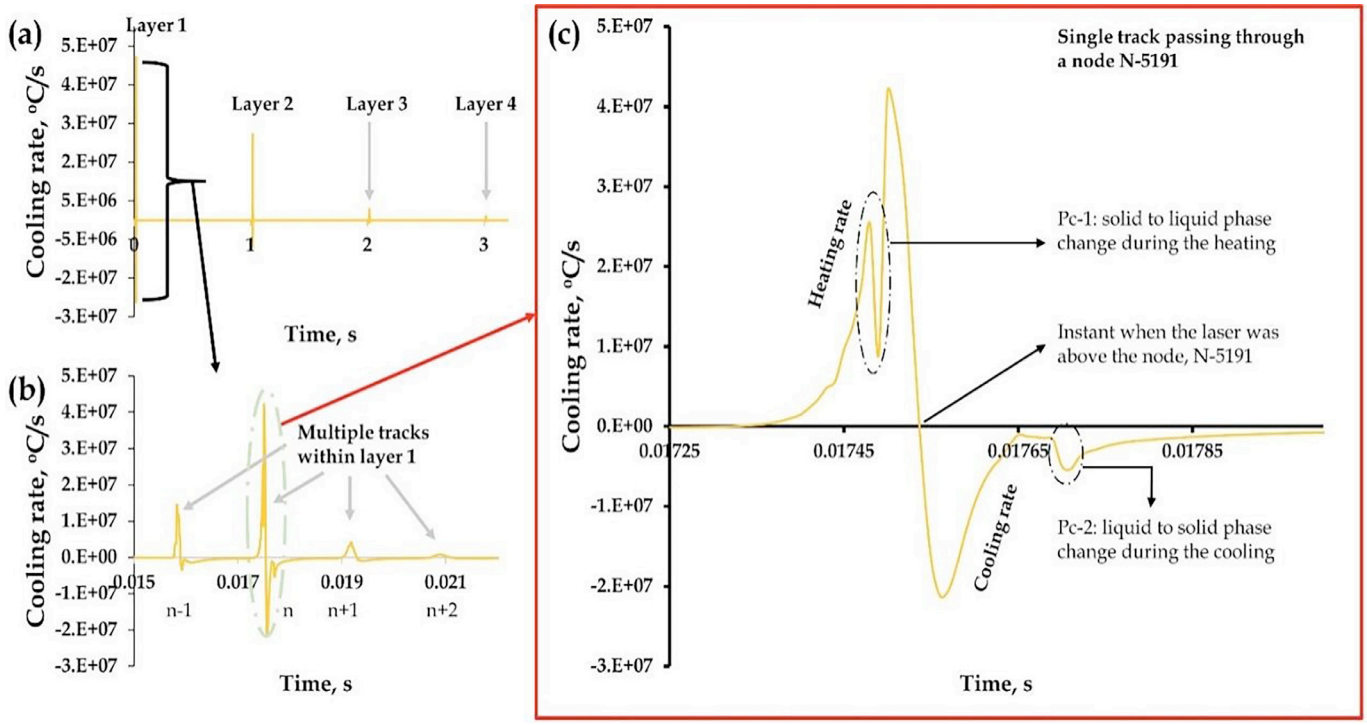

Fig. 4. Cooling rate behavior of a node (N-5191) throughout the (a) multiple layers, (b) first layer, and (c) on the middle track of the first layer.

a monitoring node, the heat rate drops because a part of it is utilized to break the intermolecular bonds of a solid powder particles into a liquid phase. Similarly, during the solidification of a molten pool, heat is released from the system, causing the cooling rate to rise slightly, which is displayed by a broader downward peak, Pc-2 [33,34]. Just before the Pc-2 phase change, the cooling rate can be seen dropping to a minimum value, which signifies a rapid cooling during a liquid phase than the solid one. The curve between the Pc-1 and Pc-2 peaks shows the molten state of a monitoring node, where nearly a third of the liquid duration is in the cooling stage.

3.2. Melt-pool: temperature behavior and melt-pool shape

The simulated thermal profile along melt pool as well as the temperature values of nodes inside a melt-pool are shown in Fig. 5. Apart from the simulated thermal profiles, the outline of a melt-pool is also drawn to denote its actual shape when the laser was above the monitored point, N-5191 on layer 1. As observed in Fig. 5(a), the melt-pool shape is considerably larger than the laser beam diameter (shown by a circle), which is 60 μm in the present case. This happens because higher heating rate adds more heat to the system than it releases through the solidified structure/substrate or surrounding powders, as evident from the comparatively lower cooling rate values. Obvious to the fact that the temperature of nodes lying directly under the laser beam will demonstrate higher temperature values than the one surrounding it, and this is clearly visible from the thermal maps corresponding to Fig. 5(a). The nodes lying outside the circle can be seen with much lower temperature values, dropping by almost 1000 °C, particularly those lying close to the melt-pool boundary. The change in thermal behavior is also considerably sharp below the laser spot but much gradual far from it. Given the Gaussian curve of the heat source, the temperature distribution across the melt-pool length, breadth, and width is similar, as seen from the attached curves.

Fig. 5(b) showsthe temperature distribution of nodes lying on the vertical plane of a melt-pool, where the temperature of nodes drops continuously. However, across the width, the temperature distribution is not symmetric because of the previously solidified region on the left, which is marked by “S” in Fig. 5(b). This causes the melt-pool to have a non-symmetric shape. The melt-pool shape can be observed non-symmetric on either plane because of the solidified and powder zone. A solidified zone provides a quick escape of heat, resulting in a relatively lower heat accumulation than the edge closer to the powder zone. As a result, nodes near the powder zone would accumulate more heat, resulting in more powder melting that would expand the melt pool shape on the powder side. Compared to only 30.8 μm half-width on the solidified side, the powder side width of a melt-pool is about 48.6 μm, nearly 50 % more extension of a melt-pool on the powder side, as seen in Fig. 6(a). This behavior can also be observed in the thermal profile in Fig. 6(a), where the thermal gradient toward the solidified region is much gradual in comparison with he sharp one observed toward the powder side. The high heat dissipation from the solidified material is the main reason for such melt pool shape i.e., high energy takeaway by solidified material reduces energy required for remelting of previous tracks and therefore melt pool is reduced on solidified side but large toward powder side where less energy is getting dissipated.

Similarly, the trailing side of a melt-pool due to the heat accumulation from the directly heated nodes can be seen about 96.4 μm in length than only 27.6 μm front end. While observing the vertical plane in Figs. 6(b, c), the melt-pool depth directly under the laser center was found to be about 39.3 μm. However, as one moves towards the laser edge in Fig. 6(c), the melt-pool depth rises to 40.4 μm. It is because of the two reasons. The first is the rapid heat transfer from surface nodes towards the bottom, and the second is the heat accumulation on the trailing side of a melt-pool due to a relatively lower heat dissipation through the substrate. This causes more material melting, especially underneath the laser edge.

3.3. Melt-pool: cooling rate behavior

Fig. 7 shows the cooling rate values of nodes lying inside a melt-pool on both the scanning and vertical planes. At an instant of a laser scanning, the monitored node, N-5191, displayed the cooling rate value of about 4.97×10^6 °C/s. The cooling rate for other nodes on the trailing side of a melt-pool can be seen first rising and then decreasing until a

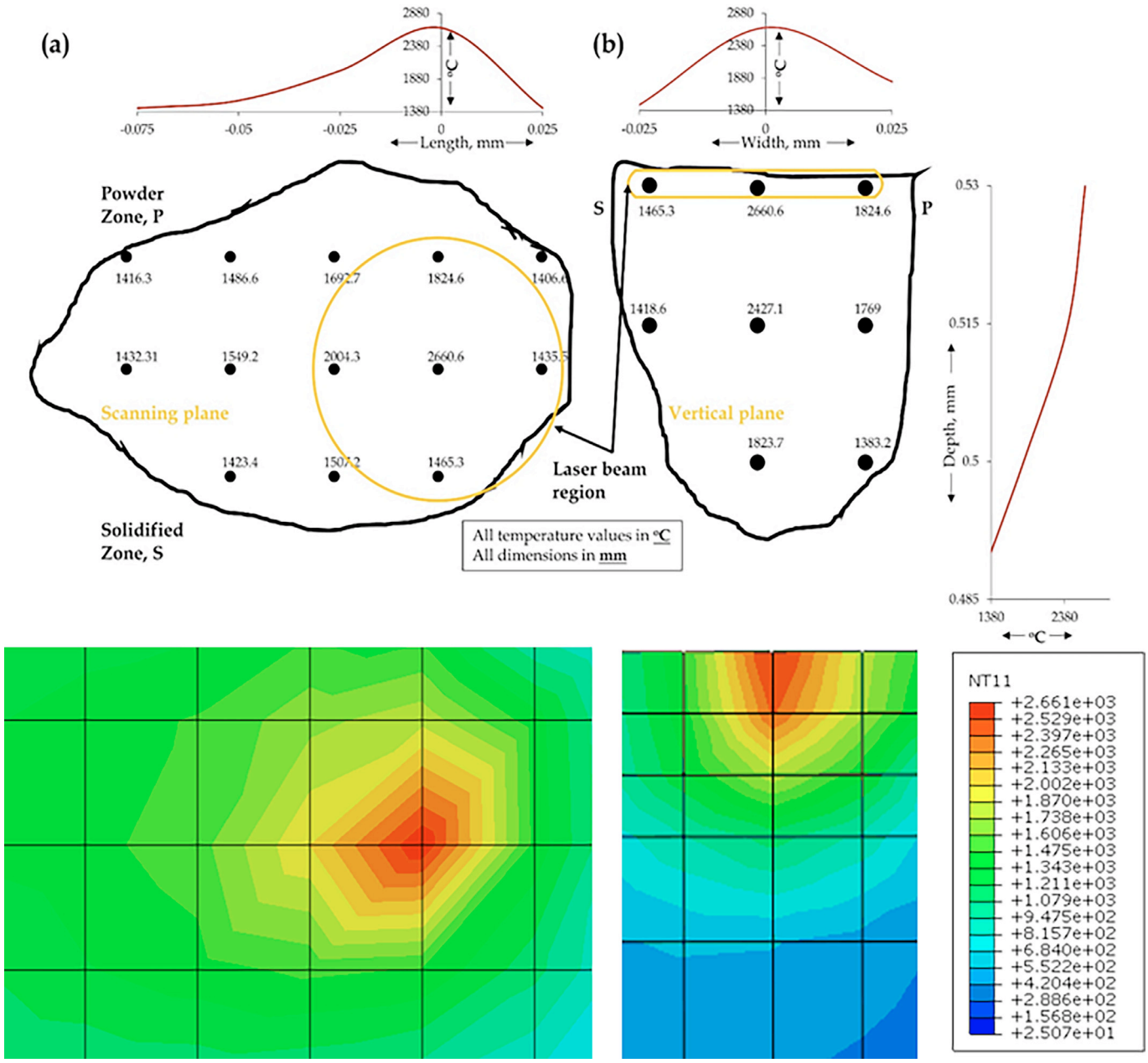

Fig. 5. Thermal profile and nodal temperature values within a melt-pool on the (a) scanning plane and (b) vertical plane; Curves describing temperature distribution across the melt-pool length, width, and depth are also provided.

solid front is reached, Fig. 7(a). The cooling rate of a node adjacent to the monitoring node on the left is approx. 16.5×10^6 °C/s, nearly 3 times higher. This shows that the maximum cooling rate for a node reaches only when the laser moves forward. This is also evident from Fig. 4 where the cooling rate rises to a maximum value when the laser left the scanning spot.

Some nodes are shown with negative cooling rate values that signifies their heating state. While evaluating the vertical plane of a melt-pool, the central nodes from top to bottom can be seen changing from the cooling to a heating mode. It is because the nodes closer to the surface dissipate heat towards the bottom, making the bottom node temperature to rise. Moreover, nodes adjacent to the powder zone, P can be seen with higher cooling rates than the one closer to the solidified zone, as shown in Fig. 7(a). Furthermore, their heating and cooling rates were both high as long as they remain in a molten state. It is because of the poor heat dissipation of the powder bed region, causing the heat to dissipate mainly through the previously solidified boundary. As a result, the nodes adjacent to the solidified zone become heated, causing a drop in a cooling rate.

Fig. 8 displays the thermal gradient values for nodes lying inside a melt-pool on both the scanning and vertical planes. Here, the thermal gradient is measured with respect to the monitoring node, N-5191. Since the monitored node is right under the laser beam, its thermal gradient value is ascribed zero. As seen from Fig. 8(a), the thermal gradient values were highest near the edge of the laser beam (represented by a circle), and then reducing towards the melt-pool front at all sides. It is because the heat addition on the trailing side is faster from nodes directly under the laser beam than it can dissipate. As a result, heat accumulation would result in a slower heat dissipation. On the vertical side, Fig. 8(b) shows the increasing temperature differential from the surface towards the melt-pool bottom. The rising temperature differential at the bottom is ascribed to the lower heating of the bottom nodes than the surface

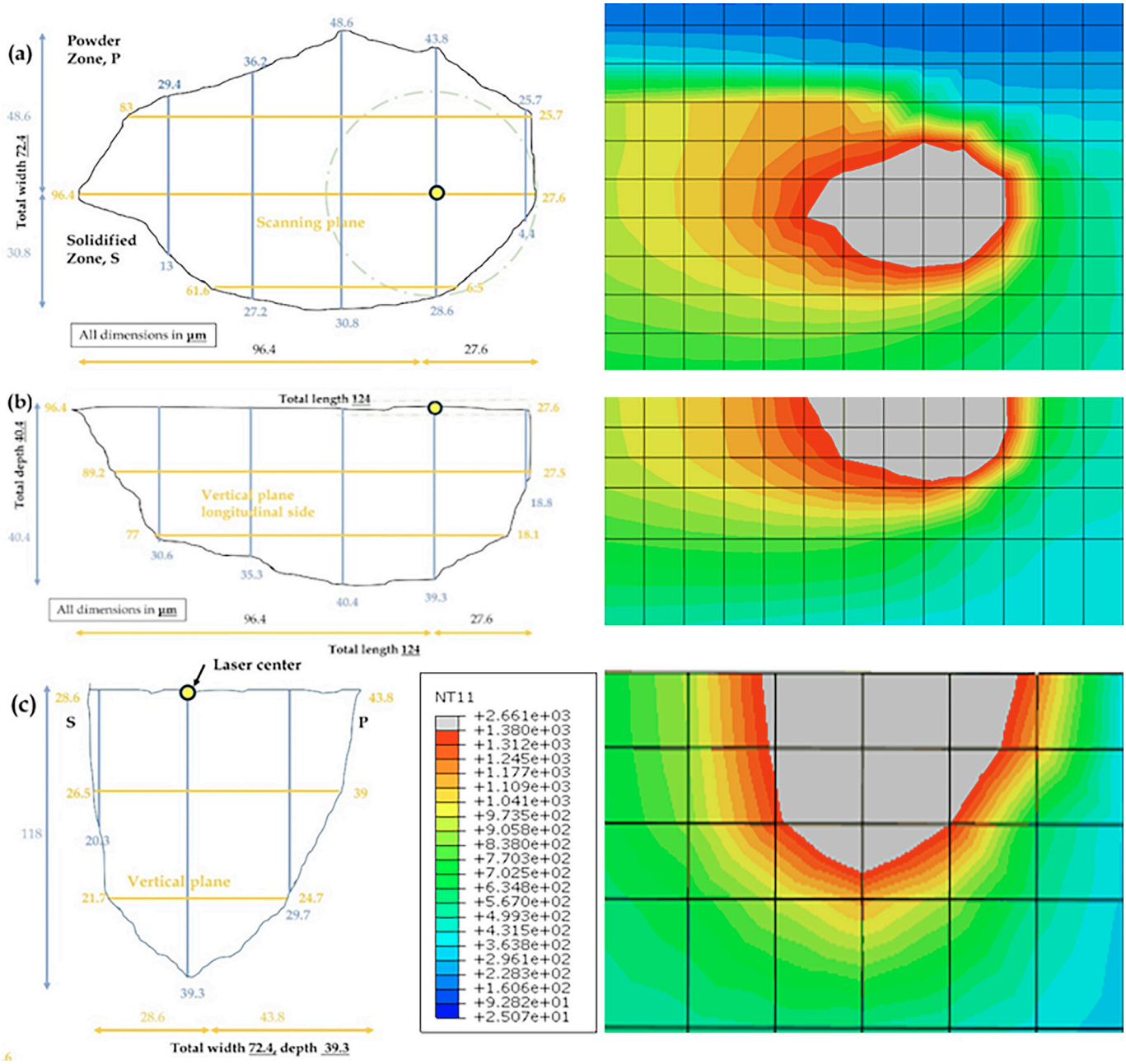

Fig. 6. Melt-pool size and shape as viewed from the (a) scanning, (b) vertical, and (c) vertical longitudinal side plane.

nodes. This shows that the heat dissipation would be faster near the bottom than the surface. While tracing the nodes at the bottom towards the trailing side of a melt-pool, the thermal gradient difference between the surface and bottom nodes keeps on decreasing due to the heat accumulation near the melt front. Compared to the melt-pool front near the solidification zone, the nodes close to the powder front can be seen with lower thermal gradient values. It is because of the faster heat transfer from nodes close to the powder bed towards the solidified end for rapid heat dissipation.

Fig. 9 shows the solidification rate distribution inside a melt-pool. Like the cooling rate and thermal gradient, solidification rate can be seen maximum near the circle in Fig. 9(a), and then reducing towards the melt-pool front at all sides. The lower solidification rate on the trailing side is associated with the high heat accumulation. The negative value of a solidification rate in Fig. 9(b) shows their instantaneous heating state due to the rapid heat transfer from the surface nodes. The bottom node will only start solidifying when the laser moves forward. It is to be noted here that the gap in the solidification rate between the surface and bottom nodes will be highest for nodes directly under the laser beam than at the trailing edge. This is because of the rapid heating and cooling of nodes under the laser beam, and then their high heat transfers towards the bottom as well as the trailing front, resulting in the heat accumulation.

4. Discussion

The laser scanning of a powder bed in the LPBF process is a complicated phenomenon due to the combination of a rapid heating and cooling cycles throughout the part fabrication, also shown in Fig. 4. The same temperature complexity can be observed inside a melt pool during the powder scanning, where a part of the melt-pool is under a heating state while the other is cooling. Moreover, the degree of heating and

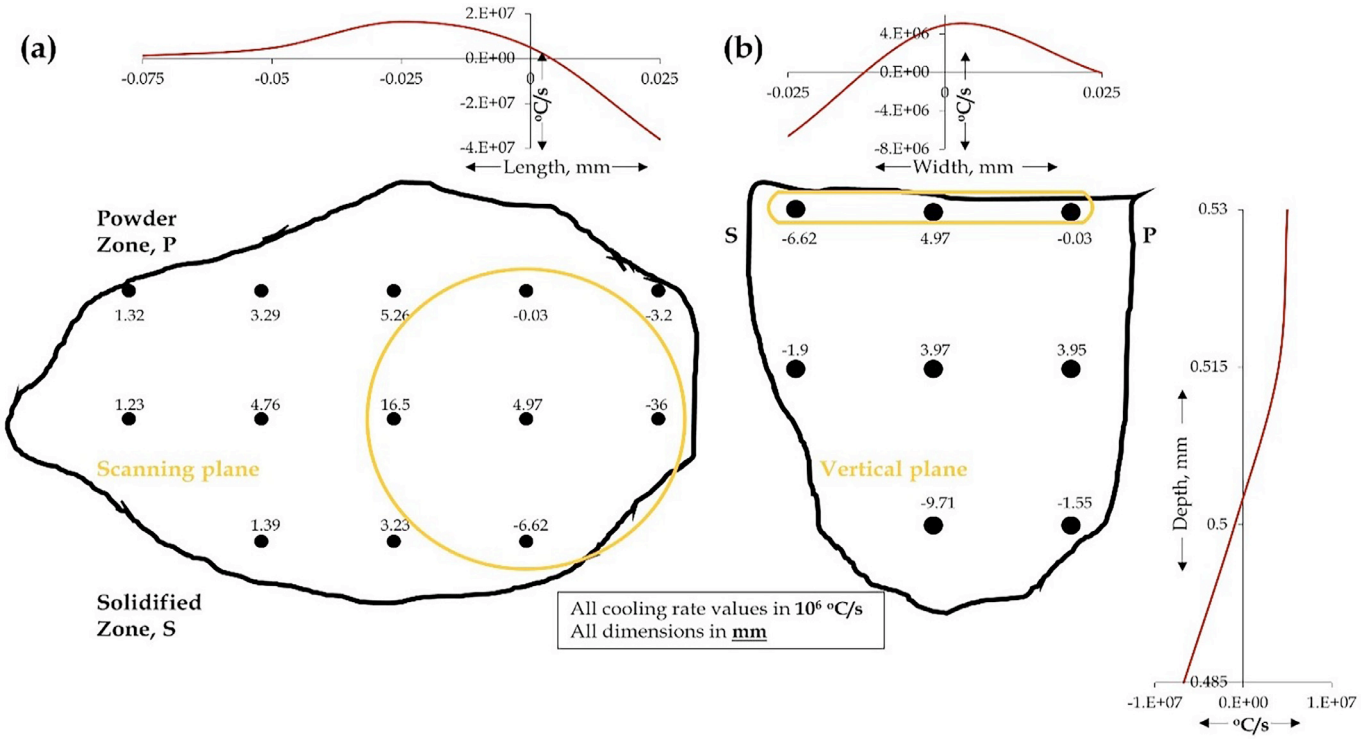

Fig. 7. Cooling rate values and curves within a melt-pool on the (a) scanning plane and (b) vertical plane.

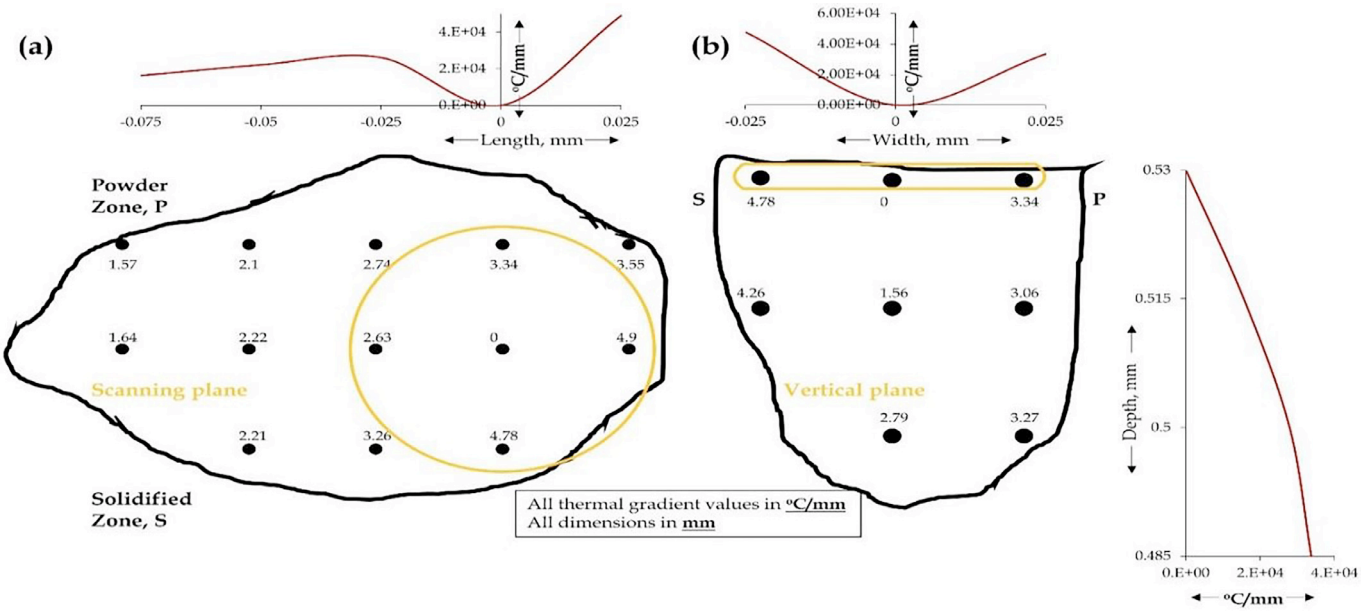

Fig. 8. Thermal gradient values and curves within a melt-pool on the (a) scanning plane and (b) vertical plane.

cooling inside a melt-pool can vary significantly, resulting in a much more complicated phenomenon. This study was intended to investigate the thermal variables distribution and evolution inside a melt-pool, as the laser scans the powder bed.

Fig. 6 demonstrates the melt-pool shape evolution based on two phenomena. The first is the heating of nodes under the direct contact of a laser beam and the other is the heat transfer from them towards the bottom or the trailing edge of a melt-pool. Fig. 4 shows the temperature of nodes near the melt front, which is above the melting point of 316L SS material. This causes the melt-pool to expand on all sides, resulting in a shape larger in size than the laser beam diameter.

The Gaussian profile of a laser beam plays a decisive role in influencing the thermal variables inside a melt-pool, like cooling rates, solidification rates, and thermal gradients. The center of the laser beam receives the maximum heat, which exponentially reduces towards the edge. Similarly, the exposed surface of a powder bed receives the maximum focus from a laser beam, which then reduces towards the depth. Compared to the node directly under the laser center, the nodes lying under the beam edge will receive much less heat. As a laser moves during the powder scanning, the node, which is once under the laser center will move towards the edge, resulting in their much higher cooling effect, as shown in Fig. 6 Similarly, thermal gradients (Fig. 8) and solidification

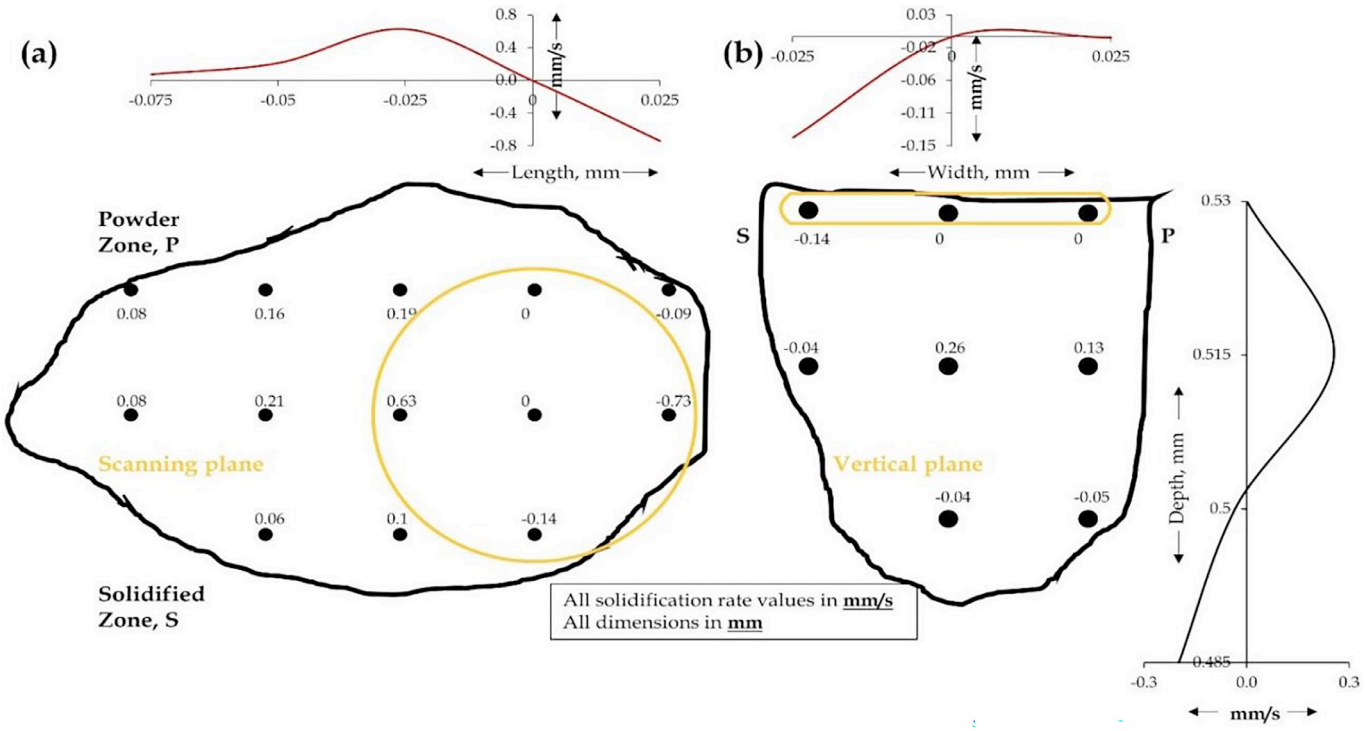

Fig. 9. Solidification rates and curves within a melt-pool on the (a) scanning plane and (b) vertical plane.

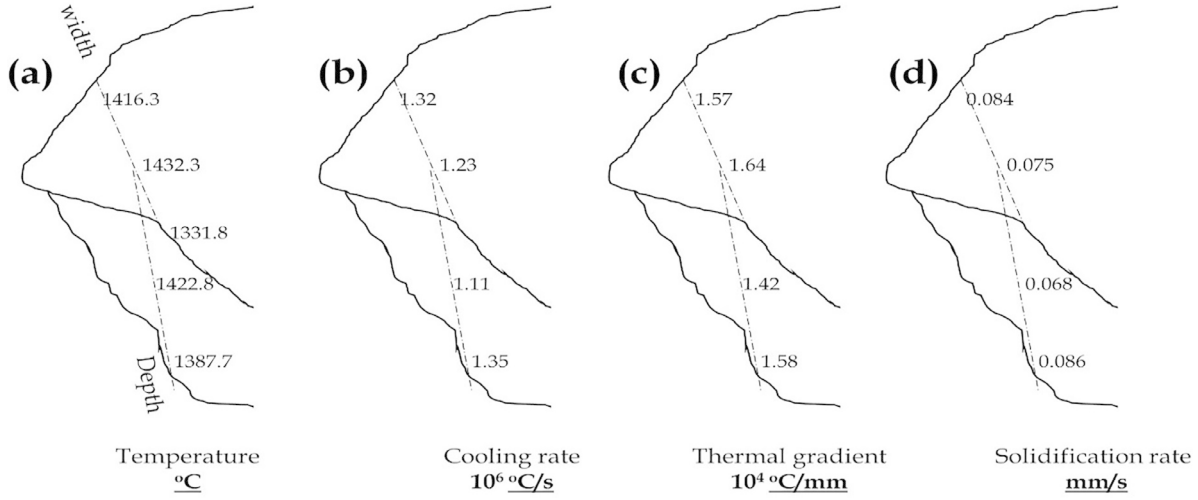

Fig. 10. Thermal variables distribution near the melt front near the trailing edge of a melt-pool.

rates (Fig. 9) of such nodes lying at the laser edge were at higher values than the node lying under the laser center or away from the laser area.

As the laser traverse ahead, the melt front also moves in the direction of a heat source. So, the node which will solidify first will be close to the melt-front. This means that their thermal variables will be the decisive factor in shaping the grain morphology. As observed from Fig. 7, the monitoring node on the powder bed was at much higher cooling rate than the bottom node. However, on the trailing side of a melt-pool, the bottom node can be seen in Fig. 10(b) with slightly higher cooling rate of 1.35×10^6 °C/s than 1.23×10^6 °C/s on the surface. This shows that finer grains can be formed near the bottom melt front as well as at the center of the melt-pool surface. Although the same physical test cannot be replicated at equivalent level due to small model dimensions related restriction, comparable behaviors can also be seen along the melt pool of LPBF fabricated 316L SS. To provide a visual indication, a representative SEM image taken from the center region i.e. mid plan of LPBF fabricated cube of 316L SS with dimensions of 5 mm × 5 mm × 5 mm size is considered. Although the dimensional scale is different, based on the observed thermal behavior along a melt pool, certain similar microstructural features can be observed in SEM image presented in Fig. 11, where tiny grain nucleates near the melt-pool border due to the elemental segregation that results in a material under cooling, and coarser grains can be seen in the middle region.

Similarly, on the scanning plane, the region close to the solidification zone is at lower cooling rate than the center. It is because of the rapid heat transfer from the powder zone as well as the melt-pool center because of easy heat escape through the solidified region. This results in a coarser grain morphology than the melt-pool center. On the contrary, a higher cooling rate was observed in nodes closer to the powder bed region that should result in finer grains than the center. However, when

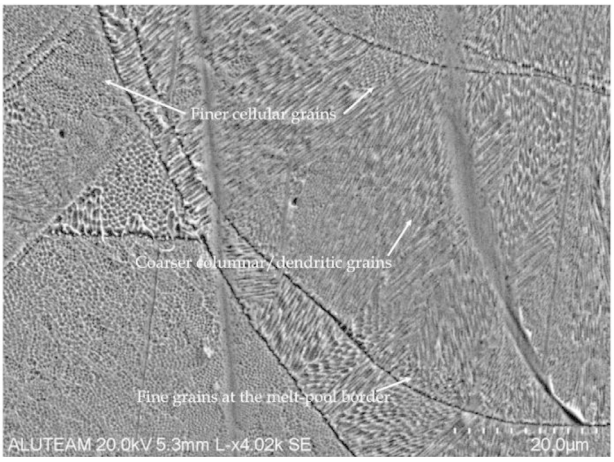

Fig. 11. Grain morphology inside a melt-pool on the vertical plane.

new adjacent tracks are scanned, the nodes adjacent to the powder zone will undergo reheating that would result in grain coarsening. As a result, a coarser grain would result on either side of the melt-pool center.

5. Conclusions

In the present work a numerical investigation of various thermal variables and their evolution inside a melt pool during the LPBF process of 316L stainless steel was performed. An accurate understanding and estimation of cooling rate, solidification rate and other variables inside a melt pool can provide the basics for the understanding of principles that govern the characteristic microstructural features of LPBF fabricated components. The obtained results also validate the selection of FEM for a detailed thermal investigation of melt pool. Some of the prominent conclusions that can be drawn from the present work are as following.

1. The melt pool temperature needs to be significantly higher than the melting temperature in order to achieve complete melting. It was also observed that during the melting of a track previous tracks achieve higher reheating temperature and often re melting in comparison with subsequent tracks mainly due to high thermal conductivity of solidified regions.
2. Both cooling rates and heating rates are significantly high during the LPBF process. However, in comparison with each other the cooling rate is considerably lower than the heating rate mainly because of the fact that heating rate is driven by external heat source, whereas cooling rate is a naturally driven phenomenon. It was also observed that cooling rate is relatively higher while metal is in liquid phase in comparison with the instance when the same region is in solid phase.
3. Melt pool size is also observed to be larger than the laser spot size and layer thickness. It was important to note that the melt pol size is larger toward the unsolidified or tracks in powder phase in comparison with the previously solidified tracks.
4. The solidification rate is also high toward the subsequent tracks i.e., tracks in powder phase in comparison with the solid phase. Along the thickness, solidifications rate is high near the top surface mainly because of exposed surface and also as the heat dissipation direction is often toward the baseplate due to its large dimensions and high heat dissipation capacity.

Declaration of competing interest

The authors declare that they have no known competing financial interests or personal relationships that could have appeared to influence the work reported in this paper.

CRediT authorship contribution statement

Saad Waqar: Writing – original draft, Software, Methodology, Formal analysis, Data curation, Conceptualization. **Hamaid M. Khan:** Writing – review & editing, Writing – original draft, Project administration, Methodology. **Aamer Nazir:** Writing – review & editing, Visualization, Validation, Resources, Funding acquisition. **Changyong Chen:** Writing – review & editing, Visualization, Validation, Software, Formal analysis. **Usama Waleed Qazi:** Writing – review & editing, Validation, Software, Data curation. **Hassan Ejaz:** Writing – review & editing, Visualization, Validation.

References

[1] Sun QD, Sun J, Guo K, et al. Influences of processing parameters and heat treatment on microstructure and mechanical behavior of Ti-6Al-4V fabricated using selective laser melting. Adv Manuf 2022;10:520–1.
[2] Majeed A, Zhang Y, Ren S, et al. A big data-driven framework for sustainable and smart additive manufacturing. Robot Comput Integr Manuf 2021;67:102026.
[3] Foteinopoulos P, Papacharalampopoulos A, Stavropoulos P. On thermal modeling of additive manufacturing processes. CIRP J Manuf Sci Technol 2018;20:66–83. doi:10.1016/j.cirpj.2017.09.007.
[4] Liu J, Song Y, Chen C, et al. Effect of scanning speed on the microstructure and mechanical behavior of 316L stainless steel fabricated by selective laser melting. Mater Des 2020;186:108355.
[5] Khairallah SA, Anderson AT, Rubenchik AM, et al. Laser powder-bed fusion additive manufacturing: Physics of complex melt flow and formation mechanisms of pores, spatter, and denudation zones. Acta Mater 2016;108(10):36–45. doi:10.1201/9781315119106.
[6] Khan HM, Waqar S, Koç E. Evolution of temperature and residual stress behavior in selective laser melting of 316L stainless steel across a cooling channel. Rapid Prototyp J 2022;28(7):1272–83. doi:10.1108/RPJ-09-2021-0237.
[7] Waqar S, Sun Q, Liu J. Numerical investigation of thermal behavior and melt pool morphology in multi-track multi-layer selective laser melting of the 316L steel. Int J Adv Manuf Technol 2021;112(3):879–95.
[8] Thijs L, Sistiaga MLM, Wauthle R, et al. Strong morphological and crystallographic texture and resulting yield strength anisotropy in selective laser melted tantalum. Acta Mater 2013;61(12):4657–68.
[9] Li S, Xiao H, Liu K, et al. Melt-pool motion, temperature variation and dendritic morphology of Inconel 718 during pulsed- and continuous-wave laser additive manufacturing: A comparative study. Mater Des 2017;119:351–60. doi:10.1016/j.matdes.2017.01.065.
[10] Vilaro T, Colin C, Bartout JD. As-fabricated and heat-treated microstructures of the Ti-6Al-4V alloy processed by selective laser melting. Metall Mater Trans A: Phys Metall Mater Sci 2011;42(10):3190–9. doi:10.1007/s11661-011-0731-y.
[11] Li X, Yi D, Wu X, et al. Effect of construction angles on microstructure and mechanical properties of AlSi10Mg alloy fabricated by selective laser melting. J Alloys Compd 2021;881:160459. doi:10.1016/j.jallcom.2021.160459.
[12] Khorasani AM, Gibson I, Awan US, et al. The effect of SLM process parameters on density, hardness, tensile strength and surface quality of Ti-6Al-4V. Addit Manuf 2019;25:176–86. doi:10.1016/j.addma.2018.09.002.
[13] Zhou L, He K, Hu Q. The effect of hatch angles on the microstructure and mechanical properties of selective laser melting 316L stainless steel. In: Proceedings of the 15th IEEE Conference on Industrial Electronics and Applications, ICIEA. Emerald Publishing Limited; 2020. p. 165–9. doi:10.1109/ICIEA48937.2020.9248216.
[14] Li Y, Zhou K, Tor SB, et al. Heat transfer and phase transition in the selective laser melting process. Int J Heat Mass Transf 2017;108:2408–16.
[15] Gusarov AV, Yadroitsev I, Bertrand P, et al. Model of radiation and heat transfer in laser-powder interaction zone at selective laser melting. J Heat Transfer 2009;131(7):072101.
[16] Mishra AK, Aggarwal A, Kumar A, et al. Identification of a suitable volumetric heat source for modelling of selective laser melting of Ti6Al4V powder using numerical and experimental validation approach. Int J Adv Manuf Technol 2018;99(9–12):2257–70. doi:10.1007/s00170-018-2631-4.
[17] Patil RB, Yadava V. Finite element analysis of temperature distribution in single metallic powder layer during metal laser sintering. Int J Mach Tools Manuf 2007;47(7–8):1069–80. doi:10.1016/j.ijmachtools.2006.09.025.
[18] Matsumoto M, Shiomi M, Osakada K, et al. Finite element analysis of single layer forming on metallic powder bed in rapid prototyping by selective laser processing. Int J Mach Tools Manuf 2002;42(1):61–7. doi:10.1016/S0890-6955(01)00093-1.
[19] Loh LE, Chua CK, Yeong WY, et al. Numerical investigation and an effective modelling on the selective laser melting (SLM) process with aluminium alloy 6061. Int J Heat Mass Transf 2015;80:288–300 Retrieved from. doi:10.1016/j.ijheatmasstransfer.2014.09.014.
[20] Heeling T, Cloots M, Wegener K. Melt pool simulation for the evaluation of process parameters in selective laser melting. Addit Manuf 2017;14:116–25.
[21] Liu Y, Zhang J, Pang Z. Numerical and experimental investigation into the subsequent thermal cycling during selective laser melting of multi-layer 316L stainless steel. Optics Laser Technol 2018;98:23–32.
[22] Zhang D, Zhang P, Liu Z, et al. Thermofluid field of molten pool and its effects during selective laser melting (SLM) of Inconel 718 alloy. Addit Manuf 2018;21:567–78.
[23] Li Z, Xu R, Zhang Z, et al. The influence of scan length on fabricating thin-walled components in selective laser melting. Int J Mach Tools Manuf 2018;126:1–12.

[24] Liu Y, Xu D, Agmell M, et al. Investigation on residual stress evolution in nickel-based alloy affected by multiple cutting operations. J Manuf Process 2021;68(PA):818–33. doi:10.1016/j.jmapro.2021.06.015.
[25] Luo X, Zhao M, Li J, et al. Numerical study on thermodynamic behavior during selective laser melting of 24CrNiMo alloy steel. Materials (Basel) 2020;13(1):45. doi:10.3390/ma13010045.
[26] Waqar S, Guo K, Sun J. Evolution of residual stress behavior in selective laser melting (SLM) of 316L stainless steel through preheating and in-situ re-scanning techniques. Opt Laser Technol 2022;149:107806. doi:10.1016/j.optlastec.2021.107806.
[27] Waqar S, Liu J, Sun Q, et al. Effect of post-heat treatment cooling on microstructure and mechanical properties of selective laser melting manufactured austenitic 316L stainless steel. Rapid Prototyp J 2020;26(10):1739–49.
[28] Bertoli US, MacDonald BE, Schoenung JM. Stability of cellular microstructure in laser powder bed fusion of 316L stainless steel. Mater Sci Eng: A 2019;739:109–17.
[29] Waqar S, Guo K, Sun J. FEM analysis of thermal and residual stress profile in selective laser melting of 316L stainless steel. J Manuf Process 2021;66:81–100. doi:10.1016/j.jmapro.2021.03.040.
[30] Tascioglu E, Khan HM, Kaynak Y, et al. Effect of aging and finish machining on the surface integrity of selective laser melted maraging steel. Rapid Prototyp J 2021;27(10):1900–9. doi:10.1108/RPJ-11-2020-0269.
[31] Chen C, Yin J, Zhu H, et al. The effect of process parameters on the residual stress of selective laser melted Inconel 718 thin-walled part. Rapid Prototyp J 2019;25(8):1359–69.
[32] Hermann Becker T, Dimitrov D. The achievable mechanical properties of SLM produced maraging steel 300 components. Rapid Prototyp J 2016;22(3):487–94.
[33] Gupta MK, Singla AK, Ji H, et al. Impact of layer rotation on micro-structure, grain size, surface integrity and mechanical behaviour of SLM Al-Si-10Mg alloy. J Mater Res Technol 2020;9(5):9506–22.
[34] Ramoni M, Shanmugam R, Ross NS, et al. An experimental investigation of hybrid manufactured SLM based Al-Si10-Mg alloy under mist cooling conditions. J Manuf Process 2021;70:225–35.